

© 2019 by Akshat Puri. All rights reserved.

MEASUREMENT OF ANGULAR AND MOMENTUM DISTRIBUTIONS OF CHARGED
PARTICLES WITHIN AND AROUND JETS IN Pb+Pb AND $p\bar{p}$ COLLISIONS AT
 $\sqrt{S_{NN}} = 5.02$ TeV WITH ATLAS AT THE LHC

BY
AKSHAT PURI

DISSERTATION

Submitted in partial fulfillment of the requirements
for the degree of Doctor of Philosophy in Physics
in the Graduate College of the
University of Illinois at Urbana-Champaign, 2019

Urbana, Illinois

Doctoral Committee:

Professor Matthias Grosse Perdekamp, Chair
Professor Anne Marie Sickles, Advisor
¹ Professor Aida El-Khadra
Professor Bryce Gadaway

Abstract

² Studies of the fragmentation of jets into charged particles in heavy-ion collisions can help in understanding
³ the mechanism of jet quenching by the hot and dense matter created in such collisions, the quark-gluon
⁴ plasma. This thesis presents a measurement of the angular distribution of charged particles around the jet
⁵ axis as measured in Pb+Pb and pp collisions collided at a center of mass energy of $\sqrt{s_{NN}} = 5.02$ TeV. The
⁶ measurement is done using the ATLAS detector at the Large Hadron Collider, and utilizes 0.49 pb^{-1} of
⁷ Pb+Pb and 25 pb^{-1} of pp data collected in 2015. The measurement is performed for jets reconstructed
⁸ with the anti- k_t algorithm with radius parameter $R = 0.4$, and is extended to regions outside the jet cone.
⁹ Results are presented as a function of Pb+Pb collision centrality, and both jet and charged-particle transverse
¹⁰ momenta. It was observed that in Pb+Pb collisions there is a broadening of the jet for charged particles with
¹¹ $p_T < 4 \text{ GeV}$, along with a narrowing for charged particles with $p_T > 4 \text{ GeV}$. Ratios between the angular
¹² distributions in Pb+Pb and pp showed an enhancement for particles with $p_T < 4 \text{ GeV}$ in Pb+Pb collisions,
¹³ with the enhancement increasing up to 2 for $r < 0.3$, and remaining constant for $0.3 < r < 0.6$. Charged
¹⁴ particles with $p_T > 4 \text{ GeV}$ show a small enhancement in the jet core for $r < 0.05$, with a growing suppression
¹⁵ of up to 0.5 for $r < 0.3$ in Pb+Pb collisions. The depletion remains constant for $0.3 < r < 0.6$.

For my Mother, Father, and Brother

Contents

| | | |
|---------------|---|----------|
| ¹⁸ | Chapter 1 Theoretical Introduction | 1 |
| ¹⁹ | 1.1 Quantum Chromodynamics | 1 |
| ²⁰ | 1.2 Heavy Ion Collisions and the Quark Gluon Plasma | 4 |
| ²¹ | 1.2.1 Heavy Ion Collisions | 4 |
| ²² | 1.2.2 The Quark Gluon Plasma | 9 |
| ²³ | 1.3 Jets and Jet Quenching | 11 |

Chapter 1

Theoretical Introduction

This section shall discuss the theoretical background necessary to understand jet measurements. It will discuss the fundamentals of quantum chromodynamics (QCD), the heavy ion collision system and the quark gluon plasma that is formed, and finally jets and jet energy loss.

1.1 Quantum Chromodynamics

Quantum Chromodynamics is a gauge theory with SU(3) symmetry that describes the dynamics of the strong interactions between quarks and gluons. It is part of the Standard Model [1], the building blocks of which are shown in Figure 1.1.

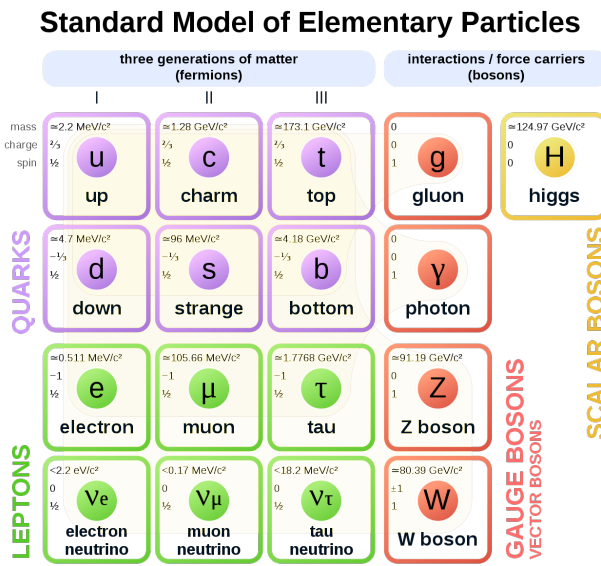


Figure 1.1: The elementary particles of the standard model.

Quarks are fermions with a spin of 1/2, and carry a fractional electric charge as well as a color charge. They all have mass and come in six flavors: up, down, top, bottom, strange, charm. The lightest quarks

³⁴ (u and d) combine and form stable particles, while the heavier quarks can only be produced in energetic
³⁵ environments and decay rapidly. Gluons are gauge bosons (force carriers) with a spin of 1, and are what hold
³⁶ quarks together. The dynamics of the quarks and gluons are described by the QCD Lagrangian given as [2]:

$$\mathcal{L}_{\text{QCD}} = \sum_q \bar{\psi}_{q,a} (i\gamma^\mu \partial_\mu \delta_{ab} - g_s \gamma^\mu t_{ab}^C \mathcal{A}_\mu^C - m_q \delta_{ab}) \psi_{q,b} - \frac{1}{4} F_{\mu\nu}^A F^{A\mu\nu} \quad (1.1)$$

³⁷ where $\psi_{q,a}$ and $\psi_{q,b}$ are quark-filled spinors for a quarks with flavor q , mass m_q , and color a and b respectively,
³⁸ with the values for a and b ranging from 1 to 3 (for the three colors). The \mathcal{A}_μ^C corresponds to the gluon field
³⁹ with C taking values from 1 through 8 (for the 8 types of gluons). The t_{ab}^C corresponds to the Gell-Mann
⁴⁰ matrices that are the generators of the SU(3) group, and dictate the rotation of the quarks color in SU(3)
⁴¹ space when it interacts with a gluon. The coupling constant is encoded within g_s , which is defined by
⁴² $g_s \equiv \sqrt{4\pi\alpha_s}$. The field tensor $F_{\mu\nu}^A$ can be written in terms of the structure constants of the SU(3) group
⁴³ f_{ABC} , and is given by:

$$F_{\mu\nu}^A = \partial_\mu \mathcal{A}_\nu^A - \partial_\nu \mathcal{A}_\mu^A - g_s f_{ABC} \mathcal{A}^B \mathcal{A}^C \quad (1.2)$$

⁴⁴ While many parallels can be drawn between Quantum Electrodynamics (QED, the theory that describes
⁴⁵ photons and electrons) and QCD, the difference between the two comes from the gluon-gluon interactions
⁴⁶ allowed in QCD, making it non-Abelian. These interactions can be summarized as shown in Figure 1.2.

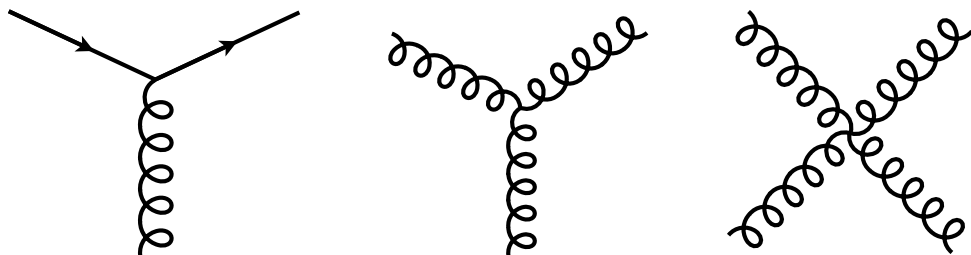


Figure 1.2: The allowed vertices in QCD. The vertices involving two or more gluons are unique to QCD and do not have a QED analog.

⁴⁷ A core feature of QCD is that the coupling constant α_s has an energy dependence shown in Figure 1.3.
⁴⁸ This dependence can be expressed in terms of the β function as

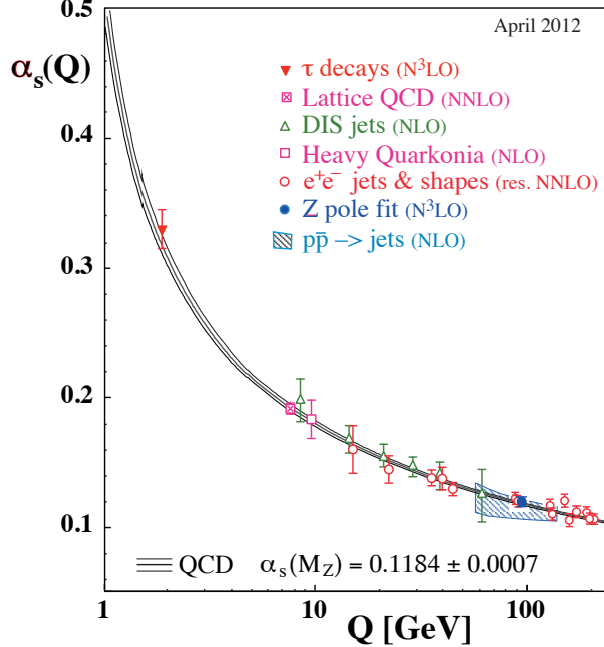


Figure 1.3: The running coupling constant α_s as a function of the momentum transfer Q . Figure taken from Ref. [2].

$$Q^2 \frac{\partial \alpha_s(Q^2)}{\partial Q^2} = \beta(\alpha_s(Q^2)) \quad (1.3)$$

49 where Q is the momentum transfer in the particle reaction. The beta function can be expressed using
50 perturbative QCD (pQCD) as

$$\beta(\alpha_s) = -(b_0 \alpha_s^2 + b_1 \alpha_s^3 + b_2 \alpha_s^4 \dots) \quad (1.4)$$

51 where the coefficients b_i depend on the number of colors and flavors.

52 This running coupling constant is small and asymptotically tends to zero at large energy scales (or at
53 small distances) and is large at small energy scales (large distances). This running coupling phenomenon
54 leads to two key behaviors: asymptotic freedom and color confinement.

55 **Asymptotic Freedom:** At high energy scales (small distances), the QCD coupling constant α_s is
56 small and tends to zero, implying a free particle behavior of quarks and gluons. This has been observed by a

57 variety of deep inelastic experiments [3–16]

58 **Color Confinement** The opposite end of the running coupling constant phenomenon is color confinement.
59 This property of QCD forbids the direct observation of free quarks and gluons, allowing only for
60 composite particles that are color singlets.

61 1.2 Heavy Ion Collisions and the Quark Gluon Plasma

62 Heavy ion collisions can be used as a tool to study the Quark Gluon Plasma [17] . They provide access to
63 the otherwise confined partons, and give insight into the QCD phase diagram and the transition between the
64 QGP and hadronic matter. This section will briefly discuss a heavy ion collision and the properties of the
65 medium that is formed in such a collision.

66 1.2.1 Heavy Ion Collisions

67 In a heavy ion collision, the colliding nuclei are accelerated to relativistic energies and are Lorentz contracted
68 discs. In the case of a Pb+Pb collision the relativistic γ factor is between 100 and 2500 for beam rapidities
69 of $y = 5.3$ and 8.5 . Each nucleus contains many colored quarks and antiquarks, with three more quarks than
70 anti-quarks per nucleon, with the $q\bar{q}$ popping in and out of the vacuum due to quantum fluctuations. These
71 $q\bar{q}$ pairs are sources of transverse color fields and the corresponding force carriers, the gluons.

72 When these pancake like discs collide, their color fields interact and there is a color charge exchange,
73 producing longitudinal color fields that fill the space between the receding discs. While the maximum energy
74 density in the process occurs just at the collision, the energy density 1 fm/c after the collision is 12 GeV/fm^3 ,
75 much higher than the 500 MeV/fm^3 in a typical hadron. Lattice QCD calculations in thermodynamics show
76 that at these energies, the partons produced in the collision cannot be treated as a collection of distinct
77 hadrons.

78 After the collision the energy density between the receding nuclei starts to decrease as the QGP cools and
79 expands. This process, seen in Figure 1.4, continues till the energy density drops to below that within a
80 hadron and the fluid “hadronizes”. These individual hadrons briefly scatter off of each other before they
81 freely fly towards the detector (freeze-out).

82 While Figure 1.4 shows snapshots of a head on (central) collision between two large nuclei, it is possible to
83 have collisions where the impact parameter is larger and hence the overlap region is smaller. These collisions,
84 called peripheral collisions, qualitatively undergo the same process described above, with the size and shape
85 of the QGP being different.

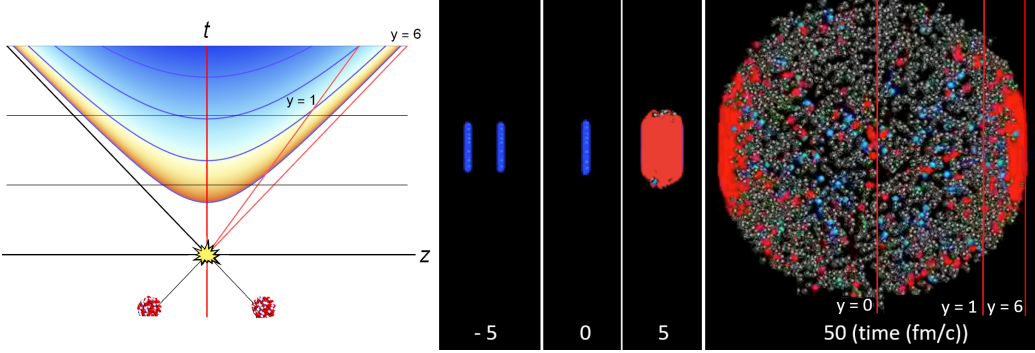


Figure 1.4: (left) Space-time diagram for a heavy ion collision. The color is indicative of the temperature of the QGP formed. (right) Snapshots of a heavy ion collision at $\sqrt{s_{NN}} = 2.76$ TeV at different times. The Lorentz contracted nuclei are in blue while the QGP is in red. Figure from Reference [18].

86 The basic parameters of a heavy ion collision such as the number of participants N_{part} and number of
87 binary collisions N_{coll} can be determined using the Glauber Monte Carlo simulations [19, 20]. This technique
88 considers a nucleus-nucleus collision as a collection of independent binary nucleon-nucleon collisions; the
89 colliding nuclei are modeled as a set of uncorrelated nucleons being positioned within the nucleus based on a
90 the nuclear density function uniform in azimuthal and in polar angles. The nuclear density function shown in
91 Figure 1.5 for Au and Cu, is given by:

$$\rho(r) = \rho_0 \frac{1 + w(r/R)^2}{1 + e^{\frac{r-R}{a}}} \quad (1.5)$$

92 where ρ_0 is the nucleon density, R is the nuclear radius, a is the skin depth, w corresponds to deviations
93 from a circular shape and is typically zero for larger nuclei like Cu, W, Au, Pb, and U. For the Pb nuclei
94 used at the LHC, $w = 0$, $R = 6.62$ fm and $a = 0.55$ fm [21].

95 They are then arranged with a random impact parameter b based on the distribution $d\sigma/db = 2\pi b$ and
96 projected onto the $x - y$ plane as shown in Figure 1.6. They are then made to travel on straight trajectories,
97 colliding if $d \leq \sqrt{\sigma_{\text{inel}}^{\text{NN}}/\pi}$, where d is the distance between the nucleons in a plane transverse to the beam
98 axis and $\sigma_{\text{inel}}^{\text{NN}}$ is the inelastic scattering cross section. [22, 23]

99 An important parameter for colliding nuclei A and B with A and B nucleons is the thickness function
100 T_{AB} . It describes the effective overlap area in which specific nucleons in the two colliding nuclei can interact.
101 It can be defined in terms of the probability per unit area of a given nucleon being located at a particular
102 distance s within the nucleus. For the colliding nuclei A and B , this is given by $T_A(\mathbf{s}) = \int \rho_A(\mathbf{s}, z_A) dz_A$ and
103 $T_B(\mathbf{s}) = \int \rho_B(\mathbf{s}, z_B) dz_B$. Then, T_{AB} is given by

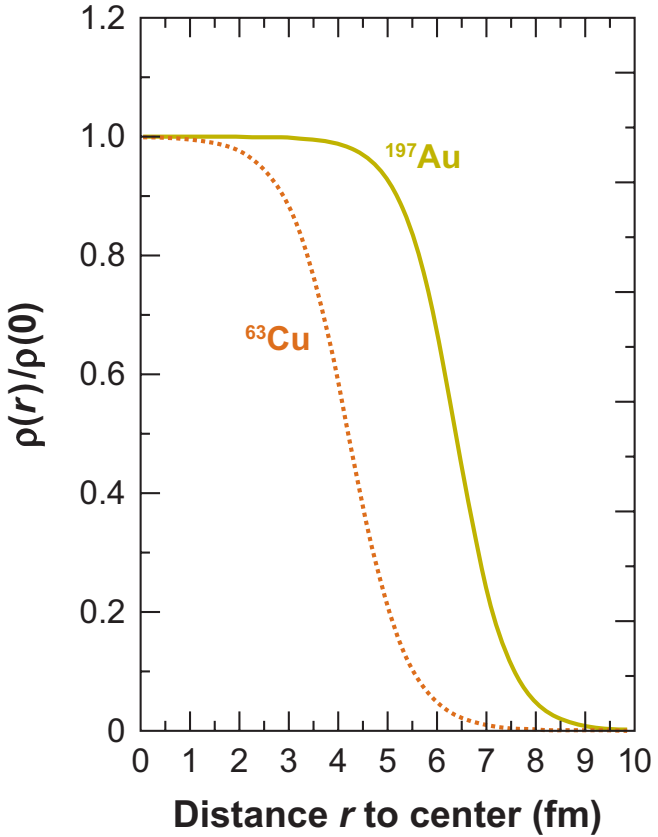


Figure 1.5: The nuclear density distributions for nuclei used at RHIC: Cu ($w = 0$, $R = 4.2$ fm and $a = 0.48$ fm) and Au ($w = 0$, $R = 6.38$ fm and $a = 0.535$ fm) [21, 22].

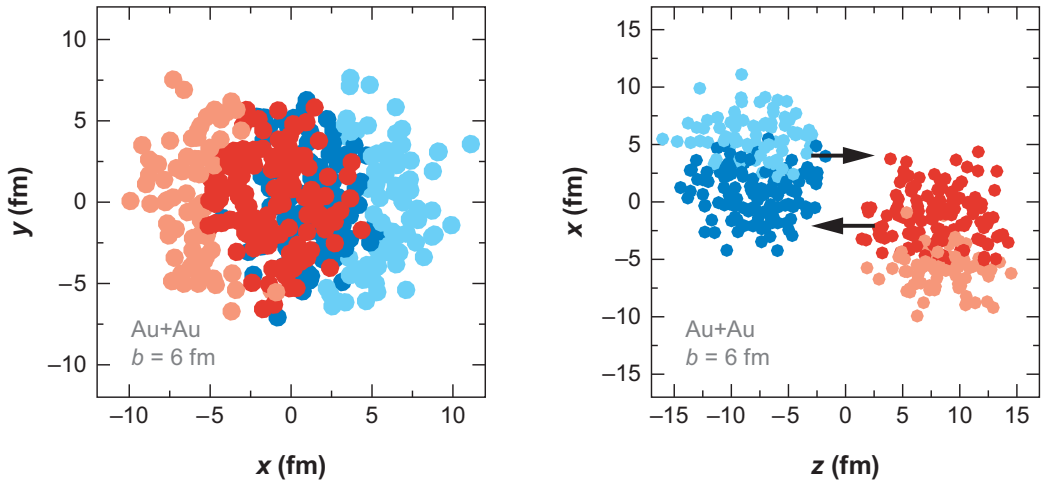


Figure 1.6: A Glauber Monte Carlo event for $Au + Au$ at $\sqrt{s_{NN}} = 200$ GeV with impact parameter of 6 fm viewed in the (left) transverse plane and (right) along the beam axis. Darker circles represent the participating nucleons. Taken from [22].

$$T_{AB}(\mathbf{b}) = \int T_A(\mathbf{s})T_B(\mathbf{s} - \mathbf{b})d^2s \quad (1.6)$$

104 The probability of then having n interactions between nuclei A and B is given by the binomial distribution:

$$P(n, \mathbf{b}) = \binom{AB}{n} \left[T_{AB}(\mathbf{b})\sigma_{\text{inel}}^{\text{NN}} \right]^n \left[1 - T_{AB}(\mathbf{b})\sigma_{\text{inel}}^{\text{NN}} \right]^{AB-n} \quad (1.7)$$

105 where the first term is the number of combinations for finding n collisions from AB possibilities, the
106 second term is the probability for having exactly n collisions, and the last term the probability of $AB - n$
107 misses. Then the total probability of an interaction between A and B is

$$\frac{d^2\sigma_{\text{inel}}^{\text{AB}}}{db^2} \equiv p_{\text{inel}}^{\text{AB}}(b) = \sum_{n=1}^{AB} P(n, \mathbf{b}) = 1 - \left[1 - T_{AB}(\mathbf{b})\sigma_{\text{inel}}^{\text{NN}} \right]^{AB} \quad (1.8)$$

108 Then the total cross section is given by

$$\sigma_{\text{inel}}^{\text{AB}} = \int_0^\infty 2\pi b db \left[1 - \left(1 - T_{AB}(\mathbf{b})\sigma_{\text{inel}}^{\text{NN}} \right)^{AB} \right] \quad (1.9)$$

109 and N_{coll} and N_{part} are given by [24, 25]

$$N_{\text{coll}}(b) = \sum_{n=1}^{AB} n P(n, b) = AB \times T_{AB}(b)\sigma_{\text{inel}}^{\text{NN}} \quad (1.10)$$

$$N_{\text{part}}(b) = A \int T_A(\mathbf{s}) \left[1 - \left(1 - T_B(\mathbf{s} - \mathbf{b})\sigma_{\text{inel}}^{\text{NN}} \right)^B \right] d^2s + B \int T_B(\mathbf{s} - \mathbf{b}) \left[1 - \left(1 - T_A(\mathbf{s})\sigma_{\text{inel}}^{\text{NN}} \right)^A \right] d^2s \quad (1.11)$$

110 The correlation between N_{coll} and N_{part} can be seen in Figure 1.7

111 The charged particle multiplicity N_{ch} along with the combination of N_{part} and impact parameter b can
112 be used to determine the centrality of a heavy ion event. An example of this is shown in Figure 1.8.

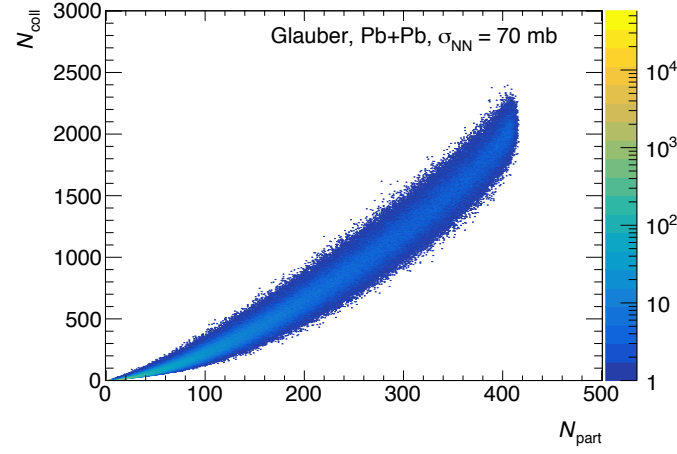


Figure 1.7: The $N_{\text{coll}} - N_{\text{part}}$ correlation for Pb+Pb collisions at $\sqrt{s_{\text{NN}}} = 5.02 \text{ TeV}$. Taken from [26].

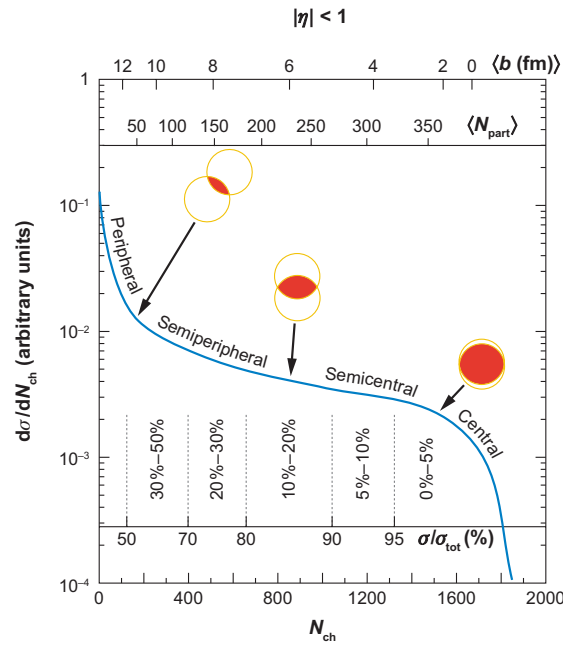


Figure 1.8: The correlation between the observable N_{ch} and N_{part} to determine the centrality distribution. Taken from [22].

1.2.2 The Quark Gluon Plasma

Extreme conditions of temperature and pressure like those in relativistic heavy ion collisions lead to the formation of the Quark Gluon Plasma [17]. It is believed to have filled the early universe a few microseconds after the Big Bang and might be present in the cores of extremely compact objects like neutron stars [27, 28]. The phase transition between the free quarks and gluons within the QGP and the confined quarks and gluons within hadrons can be seen in Figure 1.9.

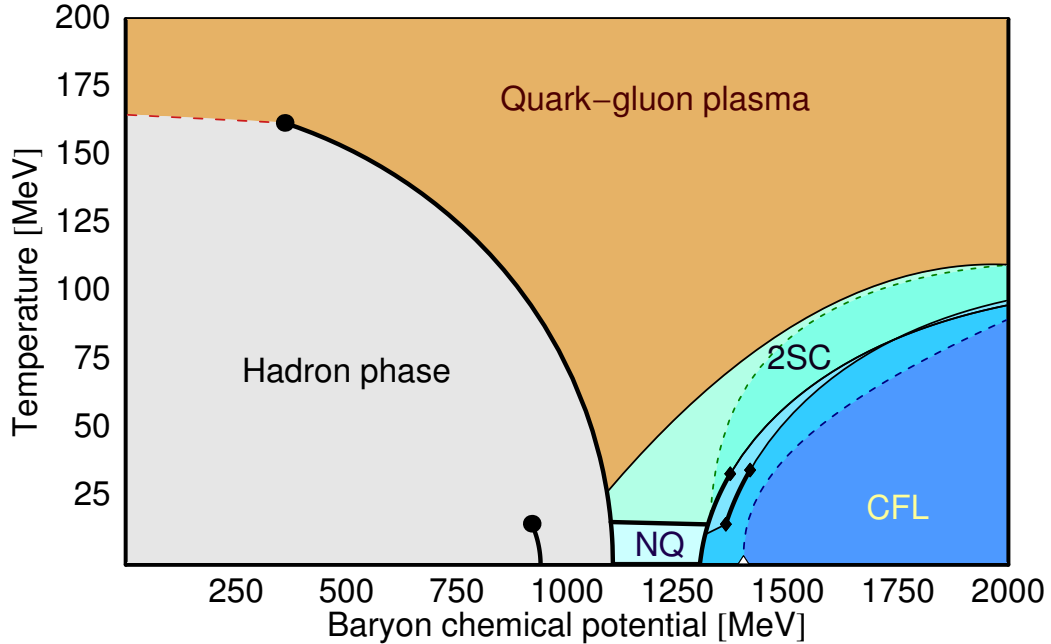


Figure 1.9: The QCD phase diagram of nuclear matter. Figure from Reference [29].

This state of matter exists for 1-10 fm/c, depending on the collision energy, above $\lambda_{\text{QCD}} = 200$ MeV, the fundamental energy scale in QCD. Thermal photons from the QGP reveal that it reaches temperatures of 300–600 MeV in central collisions at 200 GeV [30] and 2.76 TeV [31], showing very little collision energy dependence. Further, the chemical freeze-out temperature was found to be 160 MeV via measurements of ratios of final state hadrons containing the light u, d quarks [32–34] with the thermal freeze-out being 100–150 MeV [35–38]. These measurements paint a picture of the QGP being formed early in the heavy ion collision. It has a non-uniform energy density and temperature determined by the 'colliding nuclei and collision energy. The QGP then cools and expands as described by relativistic hydrodynamics, and as its temperature falls below 160 MeV, it experiences a crossover phase transition and hadronizes. This system continues to cool and expand, until at 95 GeV there is a thermal freeze-out.

The QGP was initially thought to be a weakly coupled parton gas because of asymptotic freedom from

130 QCD. The highly energetic collisions such as those at the LHC would imply a weak interaction between the
 131 quarks and gluons that make up the plasma. This would result in rare scatterings between the constituents
 132 of the gas and wash out any spatial anisotropies based on the collision geometry. On the other hand, a
 133 strong coupling within the QGP would result in the pressure gradients in the medium being driven by
 134 hydrodynamics and spatial anisotropies would be transformed to momentum anisotropies in the particles
 135 produced as shown in Figure 1.10. In this picture, the non-uniform structure of the colliding nuclei would
 136 cause a momentum anisotropy that would be further enhanced when looking at collisions that are less central
 137 and do not have perfect overlap between the colliding nuclei. These observations were seen in azimuthal
 138 correlation measurements implying that the medium is indeed strongly coupled [39–42].

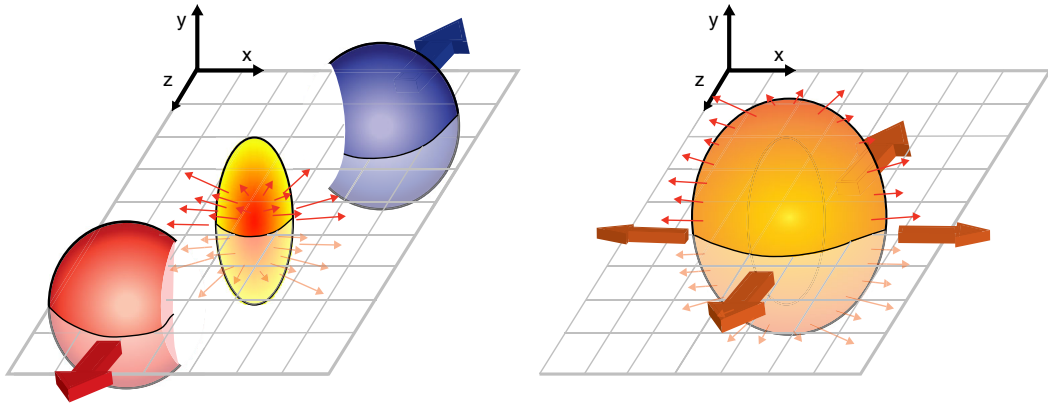


Figure 1.10: Schematic diagrams of the initial overlap region (left) and the final spatial anisotropy generated (right). Taken from [43].

139 A Fourier Transform of the angular distribution of charged hadrons in the collision debris can quantify
 140 these momentum anisotropies and give the anisotropic flow coefficients v_n , defined as [44]:

$$\frac{d\bar{N}}{d\phi} = \frac{\bar{N}}{2\pi} \left(1 + 2 \sum_{n=1}^{\infty} v_n \cos(n(\phi - \bar{\Psi}_n)) \right) \quad (1.12)$$

141 where ϕ is the angle in the transverse plane, $\bar{\Psi}_n$ are the event plane angles, and \bar{N} is the average number
 142 of particles per event. Some of these coefficients are shown in Figure 1.11. The measured anisotropies can be
 143 used to constrain the specific viscosity given by the ratio of viscosity to entropy density, η/s , and have shown
 144 that the QGP has a η/s of near the theoretical minimum of $1/4\pi$ [45].

145 The energy density of the QGP can be derived using [48]:

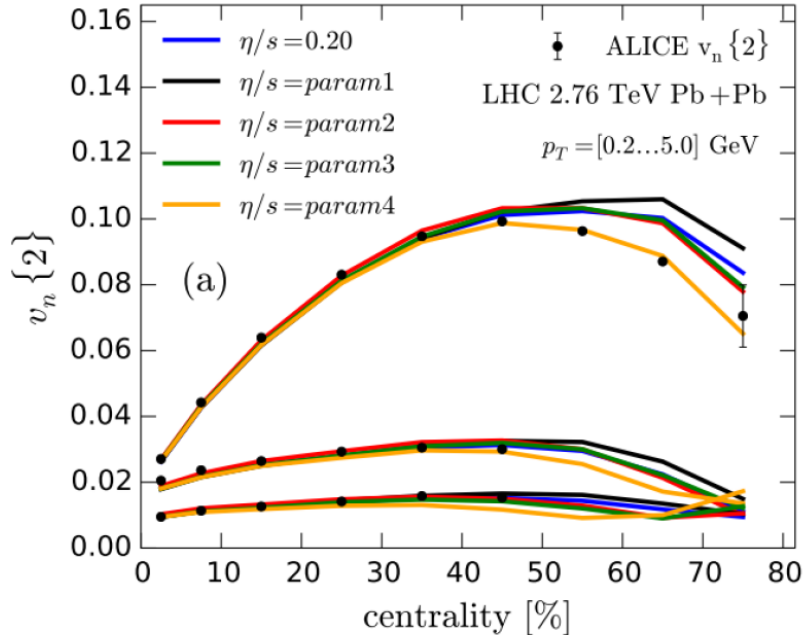


Figure 1.11: Comparison of a hydrodynamic model from [46] to anisotropy measurements by ALICE [47] for different parameterizations of η/s and for different v_n , $n = 2, 3, 4$ from top to bottom, as a function of collision centrality.

$$\varepsilon \geq \frac{dE_T/d\eta}{\tau_0 \pi R^2} = \frac{3}{2} \langle E_T/N \rangle \frac{dN_{ch}/d\eta}{\tau_0 \pi R^2} \quad (1.13)$$

where $dN_{ch}/d\eta$ is the number of charged particles produced per unity pseudorapidity, $dE_T/d\eta$ is the transverse energy per unit pseudorapidity, τ_0 is the thermalization time, R is the nuclear radius, and $E_T/N \approx 1$ GeV is the transverse energy per emitted particle. As shown in Figure 1.12, the energy density at the LHC was measured to be approximately 15 GeV/fm³, much higher than the values measured at RHIC [49, 50].

1.3 Jets and Jet Quenching

Hard scatterings in particle collisions result in the production of highly energetic partons that evolve, decay, and eventually form conical sprays of particles called jets. Jet production is well understood in the context of perturbative QCD [52], and can be shown as Figure 1.13. It can be described in terms of the parton distribution functions, scattering cross sections, and final state fragmentation functions as shown below:

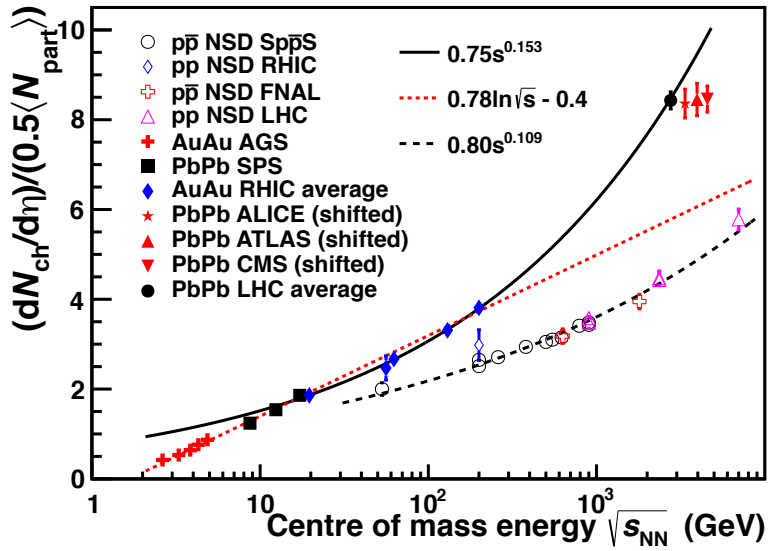


Figure 1.12: $dN_{\text{ch}}/d\eta$ per colliding nucleon pair as a function of collision energy in pp and nucleus-nucleus collisions [51].

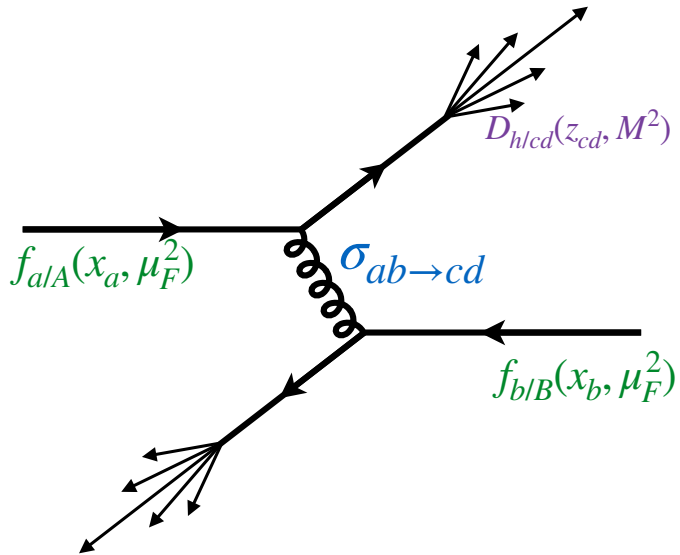


Figure 1.13: Jet production from the process $pp \rightarrow hX$, factorizing in terms of the parton distribution functions, scattering cross sections, and jet fragmentation functions. [53]

$$d\sigma_{pp \rightarrow hX} \approx \sum_{abjd} \int dx_a \int dx_b \int dz_j f_{a/p}(x_a, \mu_f) \times f_{b/p}(x_b, \mu_f) \quad (1.14)$$

$$\times d\sigma_{ab \rightarrow jd}(\mu_f, \mu_F, \mu_R) \quad (1.15)$$

$$\times D_{j \rightarrow h}(z_j, \mu_f) \quad (1.16)$$

where $x_a = p_a/P_A, x_b = p_b/P_b$ are the initial momentum fractions carried by the interacting partons, $z_j = p_h/p_j$ is the momentum fraction carried by the final observed hadron. $f_{a/p}(x_a, \mu_f)$ and $f_{b/p}(x_b, \mu_f)$ are the two parton distribution functions (PDFs), $d\sigma_{ab \rightarrow jd}(\mu_f, \mu_F, \mu_R)$ is the differential cross section for parton scattering and $D_{j \rightarrow h}(z_j, \mu_f)$ is the fragmentation function (FFs) for parton j to hadron h . μ_f and μ_F are the factorization scales and μ_R is the renormalization scale, and are typically taken to be the same hard scale Q . The PDFs characterize the initial state and represent the probability of finding a parton with momentum fraction x (shown in Figure 1.15) in the initial hadron, while the FFs describe the probability of fragmenting to a hadron h with given kinematic properties. Both the PDFs and FFs are universal and evolve via the Dokshitzer-Gribov-Lipatov-Altarelli-Parisi (DGLAP) equations [54–56].

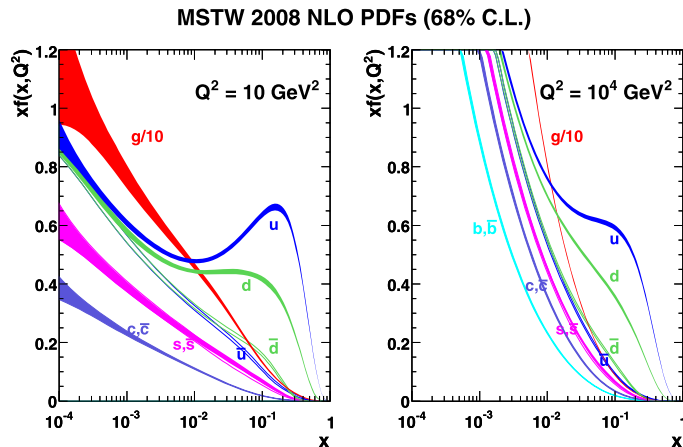


Figure 1.14: The next to leading order (NLO) PDFs at (left) $Q^2 = 10 \text{ GeV}^2$ and (right) $Q^2 = 10^4 \text{ GeV}^2$. The band is the associated one-sigma (68%) confidence level uncertainty. Taken from [57]

Figure ?? shows the inclusive jet cross section as measured by ATLAS in $\sqrt{s} = 13 \text{ TeV}$ pp collisions. In heavy ion collisions, jets must traverse the quark gluon plasma. This can result in the jet losing energy and forward momentum [59, 60], while also picking up momentum transverse to the parton direction. Jets can also deposit energy in the medium, creating a wake [61].

In a heavy ion collision where the QGP is formed, the hard scattering interactions between the partons

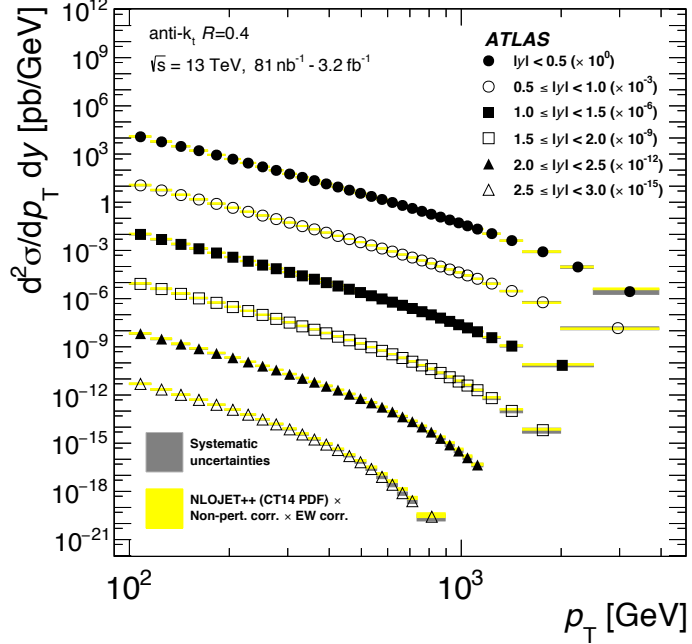


Figure 1.15: The inclusive jet cross section as a function of p_T and $|y|$ as measured by ATLAS. The data are compared to NLO pQCD calculations. Taken from [58]

¹⁶⁹ strongly interact with the QGP due to their color charge and are modified and lose energy via collisions with
¹⁷⁰ the medium constituents, or gluon bremsstrahlung.

Bibliography

- 171 [1] M. K. Gaillard, P. D. Grannis and F. J. Sciulli, *The Standard model of particle physics*, Rev. Mod.
172 Phys. **71** (1999) S96, arXiv: [hep-ph/9812285 \[hep-ph\]](#) (cit. on p. 1).
- 173 [2] J Beringer et al., *Review of Particle Physics, 2012-2013. Review of Particle Properties*, Phys. Rev. D
174 **86** (2012) 010001 (cit. on pp. 2, 3).
- 175 [3] A. Deur et al., *High precision determination of the Q^2 evolution of the Bjorken Sum*, Phys. Rev. D**90**
176 (2014) 012009, arXiv: [1405.7854 \[nucl-ex\]](#) (cit. on p. 4).
- 177 [4] J. H. Kim et al., *A Measurement of $\alpha_s(Q^2)$ from the Gross-Llewellyn Smith sum rule*, Phys. Rev. Lett.
178 **81** (1998) 3595, arXiv: [hep-ex/9808015 \[hep-ex\]](#) (cit. on p. 4).
- 179 [5] G. Altarelli et al., *Determination of the Bjorken sum and strong coupling from polarized structure
180 functions*, Nucl. Phys. **B496** (1997) 337, arXiv: [hep-ph/9701289 \[hep-ph\]](#) (cit. on p. 4).
- 181 [6] H. W. Kendall, *Deep inelastic scattering: Experiments on the proton and the observation of scaling*,
182 Rev. Mod. Phys. **63** (3 1991) 597 (cit. on p. 4).
- 183 [7] A. L. Kataev, G. Parente and A. V. Sidorov, *Improved fits to the xF_3 CCFR data at the next-to-next-to-
184 leading order and beyond*, Phys. Part. Nucl. **34** (2003) 20, [Erratum: Phys. Part. Nucl.38,no.6,827(2007)],
185 arXiv: [hep-ph/0106221 \[hep-ph\]](#) (cit. on p. 4).
- 186 [8] S. Alekhin, J. Blumlein and S. Moch, *Parton Distribution Functions and Benchmark Cross Sections at
187 NNLO*, Phys. Rev. D**86** (2012) 054009, arXiv: [1202.2281 \[hep-ph\]](#) (cit. on p. 4).
- 188 [9] S. Alekhin, J. Blumlein and S.-O. Moch, *ABM news and benchmarks*, PoS **DIS2013** (2013) 039, arXiv:
189 [1308.5166 \[hep-ph\]](#) (cit. on p. 4).
- 190 [10] J. Blumlein, H. Bottcher and A. Guffanti, *Non-singlet QCD analysis of deep inelastic world data at
191 $O(\alpha_s^3)$* , Nucl. Phys. **B774** (2007) 182, arXiv: [hep-ph/0607200 \[hep-ph\]](#) (cit. on p. 4).
- 192 [11] H1 Collaboration, *Three- and Four-jet Production at Low x at HERA*, Eur. Phys. J. C**54** (2008) 389,
193 arXiv: [0711.2606 \[hep-ex\]](#) (cit. on p. 4).

- 194 [12] ZEUS Collaboration, *Forward-jet production in deep inelastic ep scattering at HERA*, *Eur. Phys. J.*
 195 **C52** (2007) 515, arXiv: [0707.3093 \[hep-ex\]](#) (cit. on p. 4).
- 196 [13] ZEUS Collaboration, *Multi-jet cross-sections in charged current $e^\pm p$ scattering at HERA*, *Phys. Rev.*
 197 **D78** (2008) 032004, arXiv: [0802.3955 \[hep-ex\]](#) (cit. on p. 4).
- 198 [14] ZEUS Collaboration, *Inclusive dijet cross sections in neutral current deep inelastic scattering at HERA*,
 199 *Eur. Phys. J. C70* (2010) 965, arXiv: [1010.6167 \[hep-ex\]](#) (cit. on p. 4).
- 200 [15] ZEUS Collaboration, *Inclusive-jet cross sections in NC DIS at HERA and a comparison of the kT ,*
 201 *anti- kT and SIScone jet algorithms*, *Phys. Lett. B691* (2010) 127, arXiv: [1003.2923 \[hep-ex\]](#) (cit. on
 202 p. 4).
- 203 [16] H1 Collaboration, *Jet Production in ep Collisions at High Q^2 and Determination of α_s* , *Eur. Phys. J.*
 204 **C65** (2010) 363, arXiv: [0904.3870 \[hep-ex\]](#) (cit. on p. 4).
- 205 [17] E. V. Shuryak, *Quantum chromodynamics and the theory of superdense matter*, *Physics Reports*
 206 **61** (1980) 71 , ISSN: 0370-1573, URL: <http://www.sciencedirect.com/science/article/pii/0370157380901052> (cit. on pp. 4, 9).
- 208 [18] W. Busza et al., *Heavy Ion Collisions: The Big Picture, and the Big Questions*, *Ann. Rev. Nucl. Part.*
 209 *Sci. 68* (2018) 339, arXiv: [1802.04801 \[hep-ph\]](#) (cit. on p. 5).
- 210 [19] R. Glauber, *Lectures in theoretical physics*, ed. WE Brittin and LG Dunham, Interscience, New York **1**
 211 (1959) 315 (cit. on p. 5).
- 212 [20] R. Glauber et al., *Lectures in theoretical physics*, 1959 (cit. on p. 5).
- 213 [21] H. D. Vries, C. D. Jager and C. D. Vries, *Nuclear charge-density-distribution parameters from elastic*
 214 *electron scattering*, *Atomic Data and Nuclear Data Tables* **36** (1987) 495 , ISSN: 0092-640X, URL:
 215 <http://www.sciencedirect.com/science/article/pii/0092640X87900131> (cit. on pp. 5, 6).
- 216 [22] M. L. Miller, K. Reygers, S. J. Sanders and P. Steinberg, *Glauber Modeling in High-Energy Nuclear*
 217 *Collisions*, *Annual Review of Nuclear and Particle Science* **57** (2007) 205, eprint: <https://doi.org/10.1146/annurev.nucl.57.090506.123020>, URL: <https://doi.org/10.1146/annurev.nucl.57.090506.123020> (cit. on pp. 5, 6, 8).
- 220 [23] B. Alver, M. Baker, C. Loizides and P. Steinberg, *The PHOBOS Glauber Monte Carlo*, (2008), arXiv:
 221 [0805.4411 \[nucl-ex\]](#) (cit. on p. 5).
- 222 [24] D. Kharzeev and M. Nardi, *Hadron production in nuclear collisions at RHIC and high density QCD*,
 223 *Phys. Lett. B507* (2001) 121, arXiv: [nucl-th/0012025 \[nucl-th\]](#) (cit. on p. 7).

- 224 [25] A. Bialas, M. Bleszynski and W. Czyz, *Multiplicity Distributions in Nucleus-Nucleus Collisions at*
 225 *High-Energies*, Nucl. Phys. **B111** (1976) 461 (cit. on p. 7).
- 226 [26] ATLAS Collaboration, *Centrality determination in $\sqrt{s_{NN}} = 5.02 \text{ TeV Pb+Pb collision data in 2015}$* ,
 227 tech. rep. ATL-COM-PHYS-2016-1287, CERN, 2016, URL: <https://cds.cern.ch/record/2212936>
 228 (cit. on p. 8).
- 229 [27] J. C. Collins and M. J. Perry, *Superdense Matter: Neutrons or Asymptotically Free Quarks?*, Phys. Rev.
 230 Lett. **34** (21 1975) 1353, URL: <https://link.aps.org/doi/10.1103/PhysRevLett.34.1353> (cit. on
 231 p. 9).
- 232 [28] A. D. Linde, *Phase transitions in gauge theories and cosmology*, Reports on Progress in Physics **42**
 233 (1979) 389, URL: <https://doi.org/10.1088%2F0034-4885%2F42%2F3%2F001> (cit. on p. 9).
- 234 [29] S. B. Ruster, V. Werth, M. Buballa, I. A. Shovkovy and D. H. Rischke, *Phase diagram of neutral*
 235 *quark matter: Self-consistent treatment of quark masses*, Phys. Rev. D **72** (3 2005) 034004, URL:
 236 <https://link.aps.org/doi/10.1103/PhysRevD.72.034004> (cit. on p. 9).
- 237 [30] PHENIX Collaboration, *Enhanced Production of Direct Photons in Au + Au Collisions at $\sqrt{s_{NN}} =$*
 238 *200 GeV and Implications for the Initial Temperature*, Phys. Rev. Lett. **104** (13 2010) 132301, URL:
 239 <https://link.aps.org/doi/10.1103/PhysRevLett.104.132301> (cit. on p. 9).
- 240 [31] ALICE Collaboration, *Direct photon production in Pb–Pb collisions at $s_{NN}=2.76 \text{ TeV}$* , Physics Letters
 241 B **754** (2016) 235 , ISSN: 0370-2693, URL: <http://www.sciencedirect.com/science/article/pii/S0370269316000320> (cit. on p. 9).
- 243 [32] Z. Fodor and S. Katz, *Critical point of QCD at finite T and λ , lattice results for physical quark*
 244 *masses*, Journal of High Energy Physics **2004** (2004) 050, URL: <https://doi.org/10.1088%2F1126-6708%2F2004%2F04%2F050> (cit. on p. 9).
- 246 [33] STAR Collaboration, *Experimental and theoretical challenges in the search for the quark-gluon plasma: The STAR Collaboration's critical assessment of the evidence from RHIC collisions*, Nuclear Physics
 247 A **757** (2005) 102 , First Three Years of Operation of RHIC, ISSN: 0375-9474, URL: <http://www.sciencedirect.com/science/article/pii/S0375947405005294> (cit. on p. 9).
- 250 [34] ALICE Collaboration, *Production of light nuclei and anti-nuclei in pp and Pb-Pb collisions at energies*
 251 *available at the CERN Large Hadron Collider*, Phys. Rev. C **93** (2 2016) 024917, URL: <https://link.aps.org/doi/10.1103/PhysRevC.93.024917> (cit. on p. 9).

- 253 [35] PHENIX Collaboration, *Single identified hadron spectra from $\sqrt{s_{NN}} = 130$ GeV Au + Au collisions*,
 254 Phys. Rev. C **69** (2 2004) 024904, URL: <https://link.aps.org/doi/10.1103/PhysRevC.69.024904>
 255 (cit. on p. 9).
- 256 [36] BRAHMS Collaboration, *Centrality dependent particle production at $y = 0$ and $y \approx 1$ in Au+Au collisions*
 257 at $\sqrt{s_{NN}} = 200$ GeV, Phys. Rev. C **72** (1 2005) 014908, URL: <https://link.aps.org/doi/10.1103/PhysRevC.72.014908> (cit. on p. 9).
- 259 [37] PHOBOS Collaboration, *Identified hadron transverse momentum spectra in Au+Au collisions at*
 260 $\sqrt{s_{NN}} = 62.4$ GeV, Phys. Rev. C **75** (2 2007) 024910, URL: <https://link.aps.org/doi/10.1103/PhysRevC.75.024910> (cit. on p. 9).
- 262 [38] ALICE Collaboration, *Centrality dependence of π , K , and p production in Pb-Pb collisions at $\sqrt{s_{NN}} =$*
 263 2.76 TeV, Phys. Rev. C **88** (4 2013) 044910, URL: <https://link.aps.org/doi/10.1103/PhysRevC.88.044910> (cit. on p. 9).
- 265 [39] M. Aaboud et al., *Measurement of the azimuthal anisotropy of charged particles produced in $\sqrt{s_{NN}} =$*
 266 5.02 TeV Pb+Pb collisions with the ATLAS detector, Eur. Phys. J. **C78** (2018) 997, arXiv: [1808.03951](https://arxiv.org/abs/1808.03951)
 267 [nucl-ex] (cit. on p. 10).
- 268 [40] PHENIX Collaboration, *Elliptic Flow of Identified Hadrons in Au+Au Collisions at $\sqrt{s_{NN}} = 200$ GeV*,
 269 Phys. Rev. Lett. **91** (18 2003) 182301, URL: <https://link.aps.org/doi/10.1103/PhysRevLett.91.182301> (cit. on p. 10).
- 271 [41] CMS Collaboration, *Non-Gaussian elliptic-flow fluctuations in PbPb collisions at $\sqrt{s_{NN}} = 5.02$ TeV*,
 272 Phys. Lett. **B789** (2019) 643, arXiv: [1711.05594](https://arxiv.org/abs/1711.05594) [nucl-ex] (cit. on p. 10).
- 273 [42] ALICE Collaboration, *Anisotropic Flow of Charged Particles in Pb-Pb Collisions at $\sqrt{s_{NN}} = 5.02$ TeV*,
 274 Phys. Rev. Lett. **116** (13 2016) 132302, URL: <https://link.aps.org/doi/10.1103/PhysRevLett.116.132302> (cit. on p. 10).
- 276 [43] M. Connors, C. Nattrass, R. Reed and S. Salur, *Jet measurements in heavy ion physics*, Rev. Mod. Phys.
 277 **90** (2 2018) 025005, URL: <https://link.aps.org/doi/10.1103/RevModPhys.90.025005> (cit. on
 278 p. 10).
- 279 [44] A. M. Poskanzer and S. A. Voloshin, *Methods for analyzing anisotropic flow in relativistic nuclear*
 280 *collisions*, Phys. Rev. **C58** (1998) 1671, arXiv: [nucl-ex/9805001](https://arxiv.org/abs/nucl-ex/9805001) [nucl-ex] (cit. on p. 10).
- 281 [45] U. Heinz and R. Snellings, *Collective flow and viscosity in relativistic heavy-ion collisions*, Ann. Rev.
 282 Nucl. Part. Sci. **63** (2013) 123, arXiv: [1301.2826](https://arxiv.org/abs/1301.2826) [nucl-th] (cit. on p. 10).

- 283 [46] H. Niemi, K. J. Eskola and R. Paatelainen, *Event-by-event fluctuations in a perturbative QCD +*
 284 *saturation + hydrodynamics model: Determining QCD matter shear viscosity in ultrarelativistic heavy-*
 285 *ion collisions*, Phys. Rev. **C93** (2016) 024907, arXiv: [1505.02677 \[hep-ph\]](https://arxiv.org/abs/1505.02677) (cit. on p. 11).
- 286 [47] ALICE Collaboration, *Higher harmonic anisotropic flow measurements of charged particles in Pb-Pb*
 287 *collisions at $\sqrt{s_{NN}}=2.76$ TeV*, Phys. Rev. Lett. **107** (2011) 032301, arXiv: [1105.3865 \[nucl-ex\]](https://arxiv.org/abs/1105.3865)
 288 (cit. on p. 11).
- 289 [48] J. D. Bjorken, *Highly relativistic nucleus-nucleus collisions: The central rapidity region*, Phys. Rev. D
 290 **27** (1 1983) 140, URL: <https://link.aps.org/doi/10.1103/PhysRevD.27.140> (cit. on p. 10).
- 291 [49] K. Adcox et al., *Formation of dense partonic matter in relativistic nucleus-nucleus collisions at*
 292 *RHIC: Experimental evaluation by the PHENIX collaboration*, Nucl. Phys. **A757** (2005) 184, arXiv:
 293 [nucl-ex/0410003 \[nucl-ex\]](https://arxiv.org/abs/nucl-ex/0410003) (cit. on p. 11).
- 294 [50] CMS Collaboration, *Charged hadron multiplicity and transverse energy densities in PbPb collisions*
 295 *from CMS*, Journal of Physics G: Nuclear and Particle Physics **38** (2011) 124041, URL: <https://doi.org/10.1088%2F0954-3899%2F38%2F12%2F124041> (cit. on p. 11).
- 297 [51] B. Muller, J. Schukraft and B. Wyslouch, *First Results from Pb+Pb collisions at the LHC*, Ann. Rev.
 298 Nucl. Part. Sci. **62** (2012) 361, arXiv: [1202.3233 \[hep-ex\]](https://arxiv.org/abs/1202.3233) (cit. on p. 12).
- 299 [52] G. Sterman and S. Weinberg, *Jets from Quantum Chromodynamics*, Phys. Rev. Lett. **39** (23 1977) 1436,
 300 URL: <https://link.aps.org/doi/10.1103/PhysRevLett.39.1436> (cit. on p. 11).
- 301 [53] G.-Y. Qin and X.-N. Wang, *Jet quenching in high-energy heavy-ion collisions*, Int. J. Mod. Phys. E **24**
 302 (2015) 1530014, arXiv: [1511.00790 \[hep-ph\] \[hep-ph\]](https://arxiv.org/abs/1511.00790) (cit. on p. 12).
- 303 [54] G. Altarelli and G. Parisi, *Asymptotic freedom in parton language*, Nuclear Physics B **126** (1977) 298 ,
 304 ISSN: 0550-3213, URL: <http://www.sciencedirect.com/science/article/pii/0550321377903844>
 305 (cit. on p. 13).
- 306 [55] V. N. Gribov and L. N. Lipatov, *Deep inelastic e p scattering in perturbation theory*, Sov. J. Nucl. Phys.
 307 **15** (1972) 438, [Yad. Fiz.15,781(1972)] (cit. on p. 13).
- 308 [56] Y. L. Dokshitzer, *Calculation of the Structure Functions for Deep Inelastic Scattering and e+ e-*
 309 *Anihilation by Perturbation Theory in Quantum Chromodynamics.*, Sov. Phys. JETP **46** (1977) 641,
 310 [Zh. Eksp. Teor. Fiz.73,1216(1977)] (cit. on p. 13).
- 311 [57] A. D. Martin, W. J. Stirling, R. S. Thorne and G. Watt, *Parton distributions for the LHC*, The European
 312 Physical Journal C **63** (2009) 189, ISSN: 1434-6052, URL: <https://doi.org/10.1140/epjc/s10052-009-1072-5> (cit. on p. 13).

- 314 [58] ATLAS Collaboration, *Measurement of inclusive jet and dijet cross-sections in proton-proton collisions*
315 at $\sqrt{s} = 13 \text{ TeV}$ with the ATLAS detector, JHEP **05** (2018) 195, arXiv: [1711.02692 \[hep-ex\]](https://arxiv.org/abs/1711.02692) (cit. on
316 p. 14).
- 317 [59] CMS Collaboration, *Jet momentum dependence of jet quenching in PbPb collisions at $s_{NN}=2.76 \text{ TeV}$,*
318 Physics Letters B **712** (2012) 176 , ISSN: 0370-2693, URL: <http://www.sciencedirect.com/science/article/pii/S037026931200487X> (cit. on p. 13).
- 320 [60] T. A. collaboration, *Study of inclusive jet yields in Pb+Pb collisions at $\sqrt{s_{NN}} = 5.02 \text{ TeV}$* , (2017)
321 (cit. on p. 13).
- 322 [61] The CMS collaboration, *Measurement of transverse momentum relative to dijet systems in PbPb and*
323 *pp collisions at $\sqrt{s_{NN}} = 2.76 \text{ TeV}$* , Journal of High Energy Physics **2016** (2016) 6, ISSN: 1029-8479, URL:
324 [https://doi.org/10.1007/JHEP01\(2016\)006](https://doi.org/10.1007/JHEP01(2016)006) (cit. on p. 13).